Melt pond detection with Sentinel-2 and Landsat-8 in the Beaufort Gyre using Google Earth Engine

Jullian Williams[1], Jullian C B Williams[2,3], Stephen F Ackley[3], and Alberto M Mestas-Nuñez[3]

[1]Affiliation not available
[2]Department of Mathematics and Information Technology, The University of the Commonwealth Caribbean
[3]NASA Center for Advanced Measurements in Extreme Environments (CAMEE), University of Texas at San Antonio

March 25, 2024

Melt pond detection with Sentinel-2 and Landsat-8 in the Beaufort Gyre using Google Earth Engine

Jullian C.B. Williams[1,2], Stephen F. Ackley[2], Alberto M. Mestas-Nuñez[2]

[1] Department of Mathematics and Information Technology, The University of the Commonwealth Caribbean, Kingston, Jamaica.
[2] NASA Center for Advanced Measurements in Extreme Environments (CAMEE), University of Texas at San Antonio, San Antonio, TX 78249, USA.
Correspondence to: Jullian C.B. Williams (williamsjcbw@gmail.com)

Abstract

Melt pond evolution in the Arctic is an important factor in the sea-ice albedo balance and subsequent polar climate system. The spectral signature of melt ponds on Arctic ice floes is distinguishable from surrounding sea ice features in optical satellite imagery. The melt pond fraction (MPF) can be derived using a support vector machine algorithm with a class accuracy of 96%. In this paper, we provide a JavaScript-Python workflow through Google Earth Engine and Collaboratory to extract and compare the MPF from the Sentinel-2 and Landsat-8 multi-spectral instruments. We then assess the results of the onset-melt conditions in 2017 and 2020 respectively.

Introduction

Melt ponds are open water pools that form on sea ice in the warm spring and summer months (Miao et al, 2015; Rösel et al., 2011; Tschudi et al., 2008; Perovich 2002,1996). At the beginning of Summer, increasing solar radiation begins warming the snow cover over sea ice. Melt onset usually begins in June, which lowers the albedo and further enhances shortwave radiation absorption (Coakley, 2003; Fetterer, 1998). As the melting and deepening of the ponds

progress into July, a significant portion of the sea ice pack is covered with melt ponds (Fetterer, 1998). The development of these meltwater features controls the albedo of the ice surface. Indeed, the mass balance and thickness of sea ice are responsive to summertime short-wave radiation balance (Fetterer, 1998; Li et al., 2020; Perovich, 1996). The Arctic contrasts with the Antarctic in terms of its snowmelt characteristics (Willmes et al., 2014). Progression of advanced seasonal snowmelt in the Arctic is a result of persistent melt water-saturated snow in the Summer (Willmes et al., 2014; Comiso et al., 1996; Garrity, 1992). In the Antarctic, however, meltwater is confined to melt-freeze cycles in the snowpack (Willmes et al., 2014, 2006).

The Arctic Sea ice coverage is an integral factor in the Earth's surface albedo (Li et al., 2020; Callaghan et al., 2011). Sea ice albedo provides a reflecting surface for incoming solar insolation to be returned and scattered as shortwave radiation into the upper layers of the Earth's atmosphere (Perovich, 1996, 2002). A reduction in the snow-ice albedo enhances radiation absorption and promotes a surplus in the Earth's energy budget (Riihelä et al., 2013; Coakley, 2003). Melt ponds are a critical factor in the sea ice surface since they reduce the ice-albedo as they progress during the melt season (Coakley, 2003; Perovich, 1994). Indeed, the surface reflectance of melt ponds in the visible spectrum is distinguishable due to their optical properties (Perovich, 1994). These features develop at the edge of thick floes or in regions where surface topology lends itself to lateral motion of meltwater. Expectantly, water takes the path of least resistance and accumulates at the lowest elevations, draining into the ocean through crevasses or pools on thin ice. Melt ponds therefore, form in 'valleys' of ice floes where thin and flat areas exist on the floe (Fetterer, 1998). As they progress in size, they coalesce and collapse the ice structure, especially in newer ice floes (Li et al., 2020).

Melt pond detection is a matter of both reflectivity and spatial properties in the sea ice scene (Miao et al., 2015). While the pond area is distinguished primarily by its significant reduction in surface reflectance with respect to the surrounding ice cover, the shape of the pond is also important. Pond areas are distinctively rounded in shape (compactness tending towards 1) as opposed to water features with less compactness such as leads (Miao et al., 2015).

The Beaufort Gyre (Figure 1), once described as an ice production area, has shown a decrease in ice productivity with increased surface wind forcing over the last decade (Armitage et al., 2020). Water features in optical imagery are typically demarcated in the red and near-infrared bands through passive signals available to satellites (Sadeghi et al., 2015). Sentinel-2 and Landsat-8 are sun-synchronous, multi-spectral optical satellites comprised of 13 and 11 spectral bands respectively. The Sentinel-2 optical imager operates at 10, 20 and 60 meter spatial resolution with a 10-day revisit period at 290 kilometer swath width. Landsat-8 operates at a nominal spatial resolution of 30-meters and a 185 kilometer swath width. Sentinel-2 and Landsat-8 provides an unprecedented look at the sea ice cover in the Arctic, to observe and classify sea ice scenes. This paper uses the Sentinel-2 and Landsat-8 optical satellites to detect and classify melt ponds or areas where melt ponds develop on sea ice floes in the Beaufort Sea. These feature fractions, defined as the ratio between the total feature area to the ice floe area, will then be compared between satellites.

Study area and datasets

The Beaufort Sea is approximately 500,000 km^2 in surface area and roughly located ~70° – 75° N and 120° – 160 °W in the Arctic Ocean (Figure 1). The movement of ice sheets that cause pressure ridges on the ice surface, lends itself to the development of melt ponds in the

Beaufort Gyre. The weight of the pressure ridges lowers the surrounding area and creates the depressions where the ponds can develop. The instability in the cryosphere from atmospheric forcing, in tandem with the ice-albedo changes from increased melt pond prevalence in the Summer, proposes the Beaufort Gyre as a suitable study area for melt pond detection.

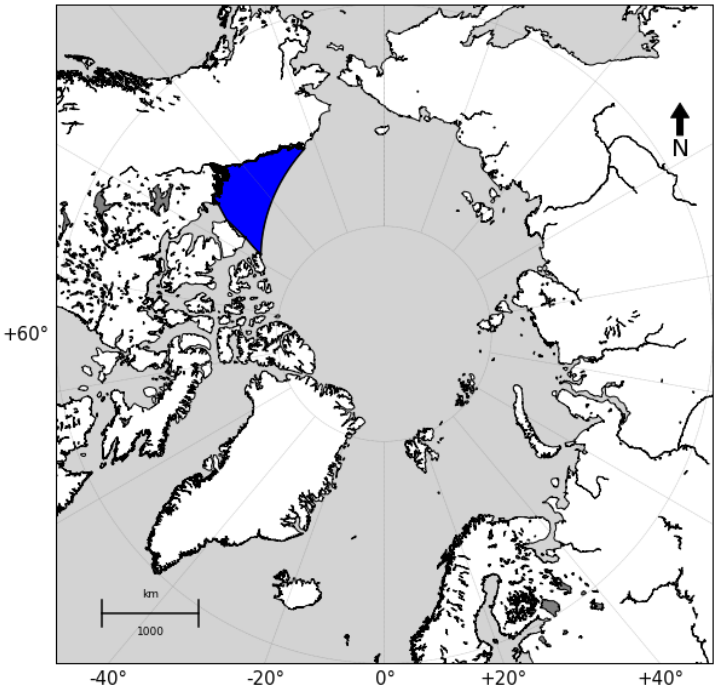

Figure 1: Lead study area offshore Barrow, Alaska. The Beaufort Sea is highlighted in blue just north of Point Barrow in the north-western segment of the map.

Landsat – 8

The Landsat-8 Operational Land Imager (OLI) satellite was launched in February 2013 and is sun-synchronous with the Earth. Landsat-8 consists of 9 spectral bands with a spatial resolution of 30 meters for bands 1 through 9. Bands 8 (panchromatic) and Bands 10/11

(Thermal infrared 1 and2) are 15 and 100 meters resolution respectively. Band 9 is used for cirrus cloud detection and is, therefore, an atmospheric correction band.

Sentinel-2

Sentinel-2 is comprised of 2 satellites, Sentinel-2A and 2B, with a third satellite (2C) to be launched in 2024. The multispectral imager proves 13 bands in the visible, near-infrared, and short-wave infrared spectrum. Sentinel-2 operates at 10, 20 and 60 meter resolutions. However, the central wavelengths of each band for Sentinel-2 and Landsat-8 are different. In fact, S2A and S2B differ in wavelength and bandwidth, although by a negligible margin (up to ~3 nm).

Methods

The 10-m spatial resolution Sentinel-2 image is resampled to the Landsat-8 (30-m) resolution for comparison between datasets. False RGB images are used instead of true color images to enhance the water bodies in the sea ice scenes. Therefore, instead of red-blue-green images, we use red-near-infrared-blue images. This increases the contrast between water features (melt pond development areas) and non-water body features (e.g. thick ice, ridges). We also use the Q60 cloud masking convention in Google Earth Engine to minimize the effects of atmospheric interference in the classification technique.

The support vector machine learning technique as described in Williams et al., (2022) is applied here to classify melt ponds in the scene. However, instead of linear features, we select circular, apparent melt features on the ice surface.

Results and Discussion

Figure 2 shows Sentinel-2 (April 20, 2017, 22:15:31 UTC) and Landsat-8 (April 20, 2017, 07:50:10 UTC) images in the Beaufort Sea.

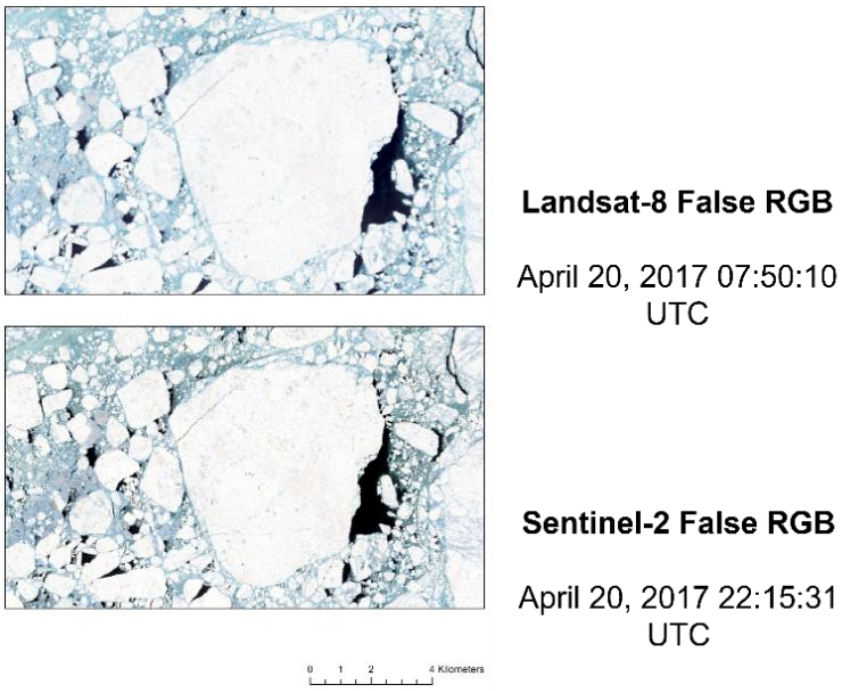

Figure 2: Landsat-8 and Sentinel-2 images showing lead and melt pond features on the surface.

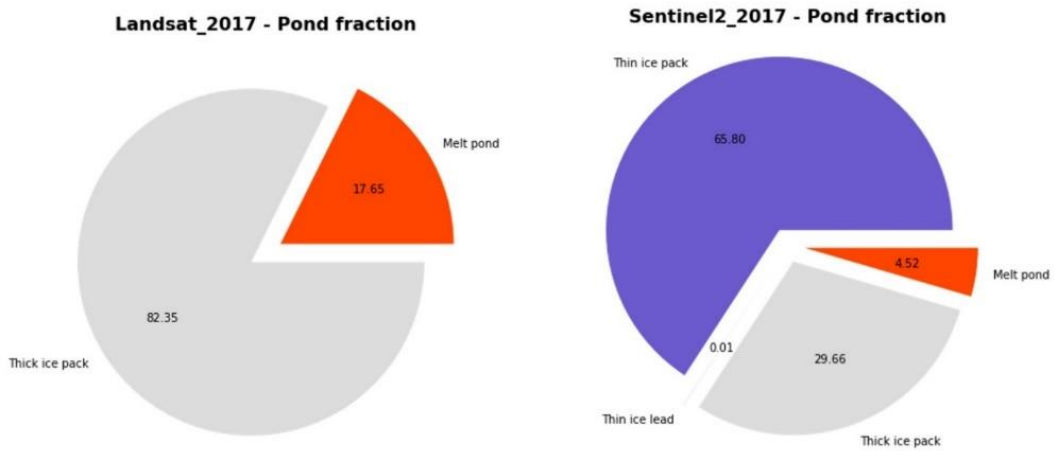

Figure 3: Melt Pond fractions from Landsat-8 and Sentinel-2 derived ice floe shown in Figure 2.

Figure 3 shows pond fractions from both images from the same ice floe. The images are trained to classify all four features in the scene. However, the Landsat-8 only detects 2 major outputs. The outputs of these melt pond fractions are a result of differences in the radiometric resolutions between imagers. Sentinel-2 has 12 bands while Landsat-8 has 11 with differing central wavelengths. Figure 4 shows the band numbers and their distributions across the scene shown in Figure 2. The x-axis displays the reflectance from 0% or no reflectance (dark – water feature) to 100% or total reflectance (bright – ice feature). While the band numbers are different (band 5 versus band 8), they describe the same range of wavelength (Near-infrared). Therefore, in figure 4, we can note the similarity in distribution of the reflectance in each band for both sensors. However, the Landsat-8 image shows more variation than the Sentinel-2 image.

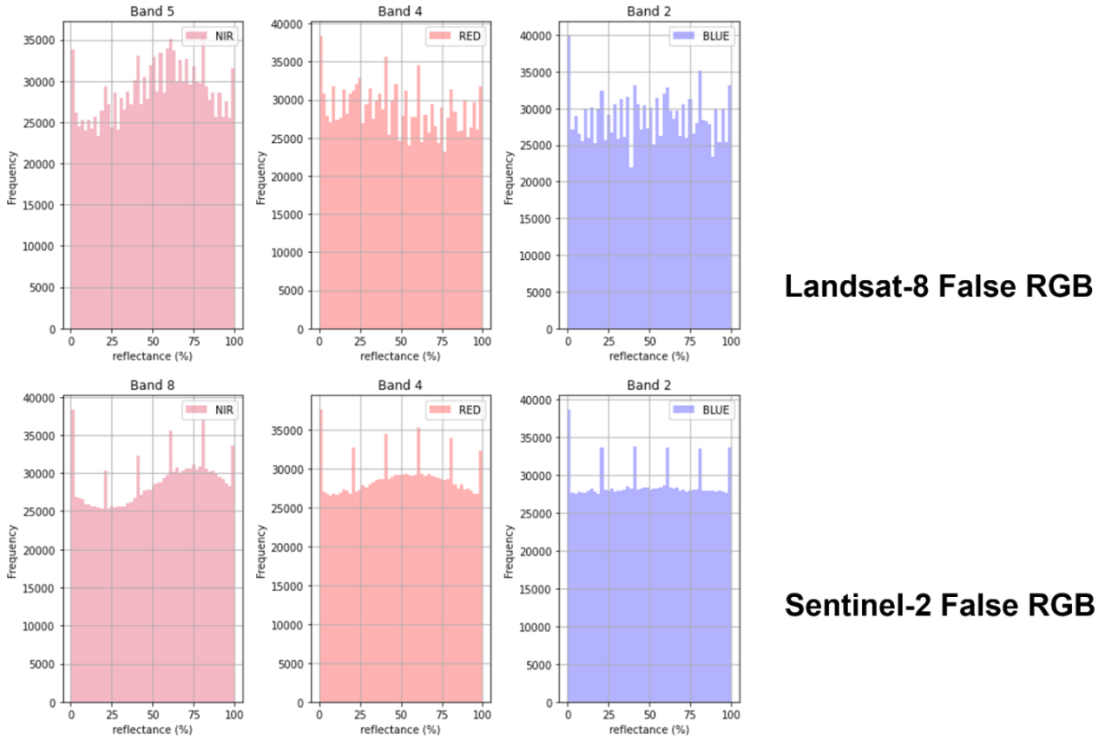

Figure 4: Band combinations in Landsat-8 and Sentinel-2 false RGB images.

Conclusion

The results from classifying the optical images show a melt pond fraction that is more than 3 times higher in the Landsat-8 image than Sentinel-2. While misclassifications in both sensors are expected from any scheme, the classification scheme was originally built to function primarily with synthetic aperture radar images. However, the classification of the Sentinel-2 optical image performs better than the Landsat-8 image. We suspect that this is a result of the difference in radiometric resolution between the optical sensors. However, because the difference in fractions is so widely different when different satellite sensors are used, the calculated effect on surface albedo calculations are profound, and care must be taken in interpreting these images in relation to the effects on the radiation balance of the ice surface for other purposes. Further study is needed, e.g. use of near-surface airborne measurements, to validate melt pond fractions obtained from these visible satellite sensors.

References

1. Callaghan, T. V., Johansson, M., Key, J., Prowse, T., Ananicheva, M., & Klepikov, A. (2011). Feedbacks and interactions: From the Arctic cryosphere to the climate system. Ambio, 40(1), 75-86.
2. Coakley, J. A. (2003). Reflectance and albedo, surface. Encyclopedia of the Atmosphere, 1914-1923.

3. Comiso, J. C., & Kwok, R. (1996). Surface and radiative characteristics of the summer Arctic sea ice cover from multisensor satellite observations. Journal of Geophysical Research: Oceans, 101(C12), 28397-28416.

4. Fetterer, F., & Untersteiner, N. (1998). Observations of melt ponds on Arctic sea ice. Journal Of Geophysical Research: Oceans, 103(C11), 24821-24835. doi: 10.1029/98jc02034.

5. Garrity, C. (1992). Characterization of snow on floating ice and case studies of brightness temperature changes during the onset of melt. Microwave remote sensing of sea ice, 545.

6. Li, Q., Zhou, C., Zheng, L., Liu, T., & Yang, X. (2020). Monitoring evolution of melt ponds on first-year and multiyear sea ice in the Canadian Arctic Archipelago with optical satellite data. Annals Of Glaciology, 61(82), 154-163. doi: 10.1017/aog.2020.24.

7. Miao, X., Xie, H., Ackley, S., Perovich, D., & Ke, C. (2015). Object-based detection of Arctic sea ice and melt ponds using high spatial resolution aerial photographs. Cold Regions Science and Technology, 119, 211-222. doi: 10.1016/j.coldregions.2015.06.014.

8. Perovich, D. (2002). Seasonal evolution of the albedo of multiyear Arctic sea ice. Journal Of Geophysical Research, 107(C10). doi: 10.1029/2000jc000438.

9. Perovich, D. (1996). The Optical Properties of Sea Ice [Ebook]. Philadelphia: US Army Corps of Engineers: Cold Regions Research & Engineering Laboratory.

10. Perovich, D. (1994). Light reflection from sea ice during the onset of melt. Journal Of Geophysical Research, 99(C2), 3351. doi: 10.1029/93jc03397

11. Riihelä, A., Manninen, T., & Laine, V. (2013). Observed changes in the albedo of the Arctic sea-ice zone for the period 1982–2009. Nature Climate Change, 3(10), 895-898. doi: 10.1038/nclimate1963

12. Rösel, A., & Kaleschke, L. (2011). Comparison of different retrieval techniques for melt ponds on Arctic sea ice from Landsat and MODIS satellite data. Annals Of Glaciology, 52(57), 185-191. doi: 10.3189/172756411795931606.

13. Sadeghi, M., Jones, S., & Philpot, W. (2015). A linear physically-based model for remote sensing of soil moisture using short wave infrared bands. Remote Sensing Of Environment, 164, 66-76. doi: 10.1016/j.rse.2015.04.007.

14. Tschudi, M., Maslanik, J., & Perovich, D. (2008). Derivation of melt pond coverage on Arctic sea ice using MODIS observations. Remote Sensing Of Environment, 112(5), 2605-2614. doi: 10.1016/j.rse.2007.12.009.

15. Williams, J. C. B., Ackley, S. F., & Mestas-Nunez, A. M. (2022). Lead Detection with Sentinel-1 in the Beaufort Gyre Using Google Earth Engine. doi:10.1002/essoar.10509955.1.

16. Willmes, S., Nicolaus, M., & Haas, C. (2014). The microwave emissivity variability of snow covered first-year sea ice from late winter to early summer: a model study. The Cryosphere, 8(3), 891-904.

17. Willmes, S., Bareiss, J., Haas, C., & Marcel Nicolaus. (2006). The importance of diurnal processes for the seasonal cycle of sea-ice microwave brightness temperatures during early summer in the Weddell Sea, Antarctica. Annals of Glaciology, 44, 297–302. doi:10.3189/172756406781811817.